Energy-loss rates of two-dimensional electrons at a GaAs/$Al_xGa_{1-x}As$ interface

Y. Ma, R. Fletcher, and E. Zaremba
Department of Physics, Queen's University at Kingston, Kingston, Ontario, Canada K7L 3N6

M. D'Iorio
National Research Council, Institute of Microstructure Sciences, Ottawa, Ontario, Canada K1A 0R6

C. T. Foxon and J. J. Harris
Philips Research Laboratories, Redhill, Surrey RH1 5HA, England
(Received 24 September 1990)

We have used low-field de Haas–Shubnikov oscillations in the resistivity to determine the electron temperatures of a two-dimensional electron gas subjected to various heating currents. This was done at many values of the electron density from 5.5×10^{15} to 10×10^{15} m^{-2} that were incrementally induced by the persistent-photoconductivity effect. The onset of second-subband occupation is clearly reflected in a large rise in energy-loss rates. The variations of the energy-loss rate with both temperature and electron density are well reproduced by detailed numerical calculations using values of deformation-potential and piezoelectric coupling parameters consistent with bulk measurements. The calculations also show that there is a transition from the low- to high-temperature behavior in the liquid-^{4}He temperature range. In this region the energy-loss rates vary roughly as the cube of the temperature, a result often observed experimentally but one which is not of fundamental significance. At the lowest temperatures the behavior should be dominated by the piezoelectric interaction which is characterized by a T^5 law. The present experimental data show the transition from T^3 to a higher-power law as the temperature is decreased, in accordance with the theoretical predictions.

I. INTRODUCTION

Low-temperature experiments on the Joule heating of a two-dimensional electron gas (2D EG) above the lattice temperature were reported at the same time as the first demonstration of 2D gases in Si metal-oxide-semiconductor field-effect transistor (MOSFET) devices.[1] The effect was detected through a decrease of the amplitude of the de Haas–Shubnikov (dHS) oscillations in the resistivity, a technique that is still widely used and employed in the present work. Since that time there have been numerous reports[2] of studies on Si inversion layers but there is still no consensus as to whether the known energy-loss mechanisms (primarily energy loss by acoustic deformation-potential coupling to the lattice) can adequately account for the experimental results.

More recently attention has focused on 2D gases in heterostructure devices. These systems have higher-quality interfaces than Si devices and one might hope for better data reproducibility. In the case of polar semiconductors one must also take into account the piezoelectric coupling of electrons to the phonons. Two groups, in particular, have had reasonable success with GaAs/$Ga_{1-x}Al_xAs$ heterojunctions in fitting experimental data with calculations based on deformation-potential and piezoelectric coupling mechanisms: Hirakawa and Sakaki[3] found good agreement for a lattice temperature $T_{ph}=4.2$ K and electron temperatures T_e up to 20 K using a deformation-potential coupling constant Z of 11 ± 1 eV, in approximate agreement with recent estimates from bulk measurements; more recently, Manion *et al.*[4] have deduced a higher value of $Z\sim16$ eV from their studies in the range $3\le T\le7$ K. This discrepancy is rather substantial since the energy-loss rates vary as Z^2. These authors suggest that the discrepancy is either due to differences in the normal modes at the junction compared to the bulk or that another unknown energy-loss mechanism is contributing. In both cases the assumption was made that the deformation potential is screened. Okuyama and Tokuda[5] have recently reanalyzed both sets of experimental data and find essentially the same results. They concluded that one should use an unscreened deformation potential but screened piezoelectric coupling, their arguments being based on the range of the two mechanisms.

Many papers[6–9] have focused on the temperature dependence of the energy-loss rate P. It is found (cf. Sec. III) that P can be well approximated by

$$P=F(T_e)-F(T_{ph}),$$

where $F(T)$ is a function characteristic of the specific electron-phonon interaction. Simple power laws are predicted for $F(T)$ in the low-temperature limit. For example, the screened deformation-potential (DP) coupling gives $F(T)\to T^7$ as $T\to0$, whereas for screened

piezoelectric (PZ) coupling $F(T) \rightarrow T^5$ in the same limit. On the other hand, when the two mechanisms are unscreened, one finds T^5 (DP) and T^3 (PZ) dependences. The low-temperature behavior is usually referred to as the Bloch limit and corresponds to the phonon wave numbers being small compared with the dimensions of the Fermi circle. At higher temperatures the temperature dependences are much weaker. Most workers in the liquid-^{4}He temperature range find a good fit to $F(T) \sim T^3$ and this has sometimes been used to suggest that unscreened piezoelectric coupling dominates in this range.[6,7] Kreschuk *et al.*[7] measured energy-loss rates in the liquid-^{4}He temperature range as the sample density was varied from single- to double-subband occupancy. They found that the power law appeared to change from T^3 to T^2 at the point where the second subband is occupied and analyzed their results in terms of piezoelectric coupling. Wennberg *et al.*[10] have found a T^5 behavior at $T \leq 0.1$ K which is consistent with screened piezoelectric coupling, though they note that their measured coefficient appears to differ from that predicted by about two orders of magnitude.

The present work deals primarily with a single-heterojunction sample which, when illuminated, shows a persistent-photoconductivity effect that raises the carrier density from 5.5×10^{15} to 10×10^{15} m^{-2}. We have extensive data from earlier experiments on this sample which show that the detailed behavior of the electron filling of the individual subbands as a function of total density is accurately represented by self-consistent electronic-structure calculations, with no adjustable parameters.[11] We therefore believe that this well-characterized sample is an ideal one with which to investigate the energy-loss mechanisms and have accordingly performed measurements of both the temperature and density dependences of the energy-loss rate. In order to provide a quantitative interpretation of our data, we have performed detailed calculations in which all parameters, apart from the magnitudes of the electron-phonon coupling constants, are fixed by the electronic-structure calculations. We have put specific emphasis on the implications of inelastic intersubband scattering which turns on as final states in the second subband become accessible. Although several calculations of the energy-loss rate in heterojunctions have appeared in the literature, there has not been a quantitative analysis of the importance of intersubband scattering, apart from our preliminary results reported elsewhere.[12]

The experimental details and analysis are presented in Sec. II and the corresponding calculations are outlined in Sec. III. We will show that both the absolute magnitude and the temperature dependence of the energy-loss rate are well described by the numerical calculations when both screened piezoelectric and deformation-potential interactions are included. We are also able to see the transition to the low-temperature (Bloch) behavior in this sample, in full accord with the numerical calculations. It is found that the T^3 dependence usually observed in the liquid-^{4}He temperature range simply marks a transition between the high- and low-temperature regimes and has no fundamental significance.

II. EXPERIMENTAL TECHNIQUES AND ANALYSIS

Experiments were carried out on two samples with single heterojunctions grown by molecular-beam epitaxy (MBE) at Philips Research Laboratories, Redhill. Details of the samples have been given elsewhere[11] but we summarize the growth details of the sample that was used for the majority of the work. A 1-μm layer of nominally undoped GaAs was first grown on a semi-insulating substrate. This was followed by a spacer layer of undoped $Al_{0.32}Ga_{0.68}As$ 16.7 Å thick, 400 Å of Si-doped (1.34×10^{24} m^{-3}) $Al_{0.33}Ga_{0.67}As$, and finally a 200-Å cap layer of GaAs. In the dark at 4.2 K, the total electron areal density n_T was $\sim 5.5 \times 10^{15}$ m^{-2} with mobility ~ 10.5 m^2 V^{-1} s^{-1} but illumination increases n_T to $\sim 10 \times 10^{15}$ m^{-2} and μ to ~ 17 m^2 V^{-1} s^{-1}. We have previously found that the subband occupations and the wave functions are sensitive to the type of light used in the illumination and in the present experiments we have chosen to work with infrared light which has been filtered to eliminate electron-hole-pair production in the GaAs. n_T was varied by short pulses of infrared radiation and was measured using the Hall resistivity in the high-field limit (see Ref. 11 for more details).

Constant currents in the range of 0.1–50 μA were provided by a battery-powered source, and potential differences were measured by a Keithley 150B microvoltmeter with 100-MΩ input impedance. The maximum Joule heating in the whole sample was < 1 μW so that the lattice temperature $T_{\rm ph}$ could always be taken to be the liquid-^{4}He bath temperature with high accuracy. The electron temperatures T_e were measured using the fact that the amplitude of the dHS oscillations in the resistivity ρ_{xx} has a temperature-dependent damping factor of the form $X/\sinh X$ with $X = 2\pi^2 k_B T_e m^*/e\hbar B$ with the usual notation, B being the flux density. Thus the ratio of the amplitudes of a particular oscillation at two temperatures serves to fix one of the temperatures if the other is known. The extrema of ρ_{xx} were determined automatically by computer as the magnetic-field sweeps were taken. This was done by simply reading the voltmeter at a rate of about 8 readings per second and saving only the maxima and minima. On data taken at higher currents (≥ 1 μA) this could be done to yield amplitudes reproducible to $\leq 0.1\%$ (provided that the oscillations were not too small). This technique is not suitable in situations of low signal-to-noise ratio, and so very-low-amplitude oscillations were avoided, as were currents less than 1 μA. This latter restriction means that at the lowest temperatures, T_e rises significantly above $T_{\rm ph}$ even at the lowest current of 1 μA, and this must be allowed for in the analysis since all actual amplitude ratios involve those taken at the lowest current and temperature. We also kept the maximum peak-to-peak oscillation amplitudes less than about 30% of the smooth background. It should also be noted that when the second subband is populated, the oscillation frequency for this band is an order of magnitude lower than for the lower subband. In these circumstances the extrema recorded are due only to the lower subband.

The experiment proceeded as follows. In some cases

we made calibration runs that entailed measuring the oscillation extrema at about ten fixed bath temperatures in the range 1.17–4.2 K. This was done at low current (1 μA for $T \leq 2$ K and up to 3 μA at 4.2 K) so that $T_{\rm ph} \simeq T_e$. The lower-temperature limit was fixed by being the lowest temperature at which we could accurately control the vapor pressure of liquid ^{4}He to better than 0.1% over long periods of time. The amplitude was taken to be the difference between any extremum and the average of the adjacent two extrema. Because the oscillation frequencies are relatively high, this should be a good approximation. After correcting the data for the expected temperature rise of T_e above $T_{\rm ph}$, to be described below, we fitted the amplitudes to the $X/\sinh X$ damping factor to extract the m^* which best reproduced all our data. Residual root-mean-square deviations of fitted and actual bath temperatures were 10–20 mK, showing that the damping factor reproduces the actual oscillation amplitudes very accurately. We detected a slight increase in m^* with electron density n_T, with a value of $0.0674m_e$ in the middle of the range. We see no significant variation of T_e with B as measured by different oscillations; any such effect is less than 1%.

The bath temperature was then fixed at 1.17 K and the oscillation amplitudes remeasured as a function of current I through the sample (using about 17 values of I). This was repeated at many values of n_T, the latter being increased incrementally by photoillumination. Using the calibration values of m^*, each amplitude was converted to T_e using the damping factor and an iterative numerical procedure. We expect the results to be accurate to the same 1% as the calibration.

It is clear that in both the calibration and the actual data, the lowest current used I_0 must give rise to an increase in T_e above $T_{\rm ph}$. This is completely negligible at $T_{\rm ph} \sim 4$ K but it becomes more serious at lower temperatures and amounts to 30–50 mK at $T_{\rm ph} \sim 1.2$ K and $I_0 = 1$ μA. This increase must be allowed for if T_e is to be obtained accurately and we do this by adopting the following procedure. We assume that a power law for the energy-loss rate P as a function of T_e and $T_{\rm ph}$ is appropriate, i.e.,

$$P = \alpha (T_e^{\gamma} - T_{\rm ph}^{\gamma}) \ . \tag{1}$$

Then the temperature increase ΔT_0 to be expected from the lowest power P_0 is given in terms of T_e obtained for any higher power P by

$$\Delta T_0 = \frac{P_0 T_{\rm ph}}{P\gamma} \left[\left[\frac{T_e}{T_{\rm ph}} \right]^{\gamma} - 1 \right] , \tag{2}$$

where we assume $\Delta T_0 \ll T_{\rm ph}$. In the first instance we assume $\Delta T_0 = 0$ and evaluate T_e for P using the ratio of the amplitudes for P and P_0; this is then used to evaluate ΔT_0 from Eq. (2) and the procedure is iterated to a final value ΔT_0. The results depend only weakly on γ; clearly, to first order $\Delta T_0 \sim P_0 (T_e - T_{\rm ph})/P$, which is independent of γ. From the published literature we expected $\gamma \sim 3$ and so we evaluated all our data on this basis. As it happened, our final results suggested a higher power but it cannot be greater than 5. If the procedures are repeated using $\gamma = 5$, we find shifts of < 10 mK compared to $\gamma = 3$; these are comparable with our calibration uncertainties and so have not been incorporated.

For any particular n_T there is usually a variation of the smooth background resistivity with magnetic field and, because we have used constant current, this leads to variation in the Joule heating. We have corrected all the data to constant power—in fact, the power at $B = 0$—using interpolation between data sets taken at different powers and adopted the average over all the different oscillation values as the best estimate of T_e. When only a single subband is occupied, the variation of T_e with oscillation number is always less than 1% and so the averaged T_e is accurate to no worse than 1%. However, for $n_T \geq 8.5 \times 10^{15}$ m^{-2}, the second subband has its own set of dHS oscillations, of much longer period than the first, and this leads to a strong variation of T_e which is in antiphase with these long-period oscillations in ρ_{xx}. Figure 1 shows an example of this behavior and clearly indicates that the energy-loss rate is strongly affected by the density of states at the Fermi energy. This is presumably also true for the lower-subband oscillations and it is perhaps a little surprising that in the single-band case the measurements of T_e for different oscillation numbers are so independent of the oscillation amplitude (over at least a factor of 3 in the amplitude). In the two-band case we take as the best estimate of T_e the average over all the useful oscillations. The ideal case would be to average over a complete upper-subband oscillation, but it was usually possible to obtain data for at most one-half oscil-

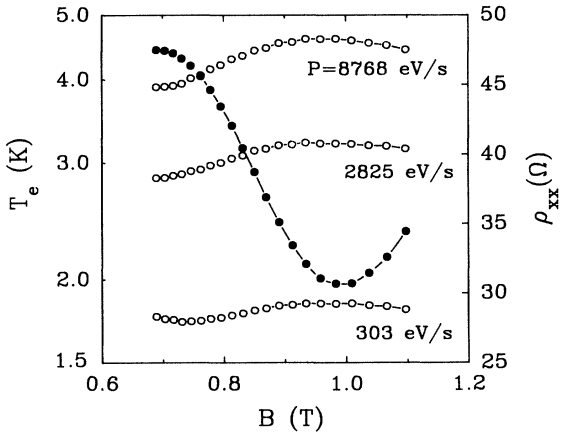

FIG. 1. A comparison of the measured average resistivity ρ_{xx} (solid symbols and right-hand axis) and the measured electron temperature T_e (open symbols and left-hand axis which is on a logarithmic scale) appropriate to three fixed electron input powers as a function of magnetic field at $n_T = 9.55 \times 10^{15}$ m^{-2}. ρ_{xx} is determined from the midpoints of the dHS oscillations of the lower-subband electrons and the partial oscillation seen here is due to the electrons in the upper subband. The variation of T_e is in antiphase with that of ρ_{xx} and shows that the energy-loss rate is affected by changes in the density of states at the Fermi energy.

lation (including a minimum and a maximum). Hence for these values of n_T the energy-loss rates could be much more uncertain than at lower n_T.

Finally, we would like to mention an auxiliary experiment which was carried out to check that the temperatures of the electrons in the two bands are the same, as is assumed to be the case in the calculation. This experiment was actually done on another sample of similar characteristics, but which had more electrons in the upper subband when the persistent-photoconductivity effect was close to saturation; this gave us about twice as many oscillations for the upper-subband electrons which allowed a more accurate analysis to be made. The dHS oscillations $\tilde{\rho}_{xx}$ were recorded on a scale linear in $1/B$. Using filtering of the Fourier transforms, the data were separated into the oscillations appropriate to the individual subbands. The set of oscillations for the upper subband was then analyzed (assuming the same m^* as obtained for the lower subband) by fitting all the data points, not just the extrema, to the full expression of the dHS oscillations, i.e.,

$$\tilde{\rho}_{xx}=A_0\frac{X}{\sinh X}\exp\left[\frac{-2\pi^2 k_B T_D m^*}{\hbar eB}\right]\cos\left[\frac{2\pi f}{B}+\phi\right], \tag{3}$$

where T_D is the Dingle temperature, f is the oscillation frequency, and ϕ and A_0 are constants and were obtained from a fit to the experimental data at 1.17 K. This technique should give a much more accurate value for T_e than simply fitting the extrema of the oscillations because it involves all the data points (≈ 200) rather than the few (~ 6) extrema values. For three input powers we obtained three electron temperatures of 1.47, 2.15, and 3.21 K. The average electron temperatures for the lower-subband electrons (using the usual analysis with 20–30 values of the extrema) were 1.47 K (this value was incorrectly reported as 1.57 K in Ref. 12), 2.13 K, and 3.29 K, which are in excellent agreement and show that the electrons in the two subbands are in good thermal equilibrium.

III. THEORY

Our starting point is the usual assumption of weak coupling between the electronic and lattice degrees of freedom. With this assumption, the energy-loss rate can be calculated using lowest-order time-dependent perturbation theory (Fermi's golden rule) as first demonstrated for bulk semiconductors by Kogan.[13] The approach is well suited to problems of this kind and has been applied to other situations, such as Kapitza resistance.[14] In all such applications, the subsystems between which energy is being exchanged are each assumed to be in internal thermal equilibrium with a distinct temperature. In the present context, the lattice (i.e., the phonon system) is maintained at the temperature $T_{\rm ph}$ by means of an external heat bath (liquid ^{4}He). The electrons, however, are maintained at a higher temperature T_e through resistive Joule heating. Implicit in this picture is that electron-electron interactions are sufficiently strong to ensure rapid equilibration within the electronic system of the energy extracted from the external electric field. The magnitude of the steady-state temperature difference between the electron and phonon subsystems is finally established by the strength of the electron-phonon coupling.

The electron-phonon energy-transfer rate is given by the expression

$$P=\sum_{if}\rho_i(E_f^{\rm ph}-E_i^{\rm ph})w_{i\to f}\ , \tag{4}$$

where $w_{i\to f}$ is the Fermi golden-rule transition rate

$$w_{i\to f}=\frac{2\pi}{\hbar}|\langle f|H_{e\text{-ph}}|i\rangle|^2\delta(E_i-E_f)\ . \tag{5}$$

Here $H_{e\text{-ph}}$ is the electron-phonon interaction, to be specified, which induces transitions from the initial state $|i\rangle$ with energy $E_i=E_i^e+E_i^{\rm ph}$ to the final state $|f\rangle$ with energy $E_f=E_j^e+E_f^{\rm ph}$. Finally, the initial-state density matrix ρ_i is assumed to have the form

$$\rho_i=\rho^e(T_e)\rho^{\rm ph}(T_{\rm ph})\ , \tag{6}$$

i.e., a product of canonical distributions at the subsystem temperatures T_e and $T_{\rm ph}$.

To evaluate Eq. (4), we must specify in more detail the model of the heterojunction to be used. Regarding the phonons, we shall make the simplifying assumption[4,15,16] that the lattice modes can be approximated by the bulk modes of GaAs, the material to which the 2D EG is mainly confined. This effectively neglects the elastic inhomogeneities at the interface, but is not a bad approximation for $Al_xGa_{1-x}As/GaAs$ heterostructures since the elastic properties of the two materials are not too dissimilar.[17] In any event, since the total energy-transfer rate is a sum over all possible lattice modes, one would not expect details associated with the reflection and refraction of elastic waves, or the possible existence of localized modes,[18] to affect significantly our estimate of the energy-loss rate.

In III-V semiconductor compounds, electrons couple to phonons via the deformation-potential and piezoelectric interactions. Both of these interactions can be represented in the form

$$H_{e\text{-ph}}=\sum_{\vec{q},\lambda}M_{\vec{q}\lambda}\hat{n}_{-\vec{q}}(a_{\vec{q}\lambda}+a^{\dagger}_{-\vec{q}\lambda})\ , \tag{7}$$

where $\vec{q}$ and λ are the (bulk GaAs) phonon wave vector and polarization, respectively; $a_{\vec{q}\lambda}$ is the annihilation operator for phonons with frequency $\omega_{\vec{q}\lambda}$; and $M_{\vec{q}\lambda}$ is an electron-phonon matrix element which depends on the specific form of the interaction. The remaining quantity $\hat{n}_{\vec{q}}$ is the Fourier transform of the electron-density operator. With this form of the interaction, Eq. (4) reduces to[13]

$$P=\frac{2}{N}\sum_{\vec{q},\lambda}|M_{\vec{q}\lambda}|^2\omega_{\vec{q}\lambda}\chi''(\vec{q},\omega_{\vec{q}\lambda})[N_e(\omega_{\vec{q}\lambda})-N_{\rm ph}(\omega_{\vec{q}\lambda})]\ , \tag{8}$$

where $\chi''(\vec{q},\omega)$ is the absorptive part of the electron-density response function and

$$N_i(\omega)=(e^{\hbar\omega/k_B T_i}-1)^{-1}$$

is the Bose factor at temperature T_i. If several distinct electron-phonon interactions are relevant, Eq. (8) is understood to be summed over all such interactions (provided that interference terms in the squared matrix element do not contribute). The factor of 2 in Eq. (8) appears because of our definition of $\chi''(\vec{q},\omega)$ (*not* because of electron spin) and N, the total number of electrons in the 2D EG, is introduced to define the power dissipation *per* electron.

At low temperatures only acoustic modes are important and these are represented within a Debye model. As such, the phonons have frequencies $\omega_{\vec{q}\lambda}=s_\lambda q$ where the index distinguishes one longitudinal ($\lambda=l$) and two degenerate transverse ($\lambda=t$) branches. The phonon wave vector $\vec{q}$ has components parallel ($q_\parallel$) and perpendicular ($q_\perp$) to the heterojunction interface. The summation over $\vec{q}$ in Eq. (8) can be converted to an integral in which $q_\parallel$ and ω appear as integration variables. We then obtain for the energy-loss rate the expression

$$P=\frac{1}{N}\int_0^\infty d\omega\,\omega^2[N_e(\omega)-N_{\rm ph}(\omega)] \times\sum_\lambda \frac{1}{s_\lambda\pi^2}\int_0^{\omega/s_\lambda} dq_\parallel \frac{q_\parallel}{(\omega^2-s_\lambda^2 q_\parallel^2)^{1/2}} \times\overline{|M_{\vec{q}\lambda}|^2}\chi''(\vec{q},\omega)\ . \tag{9}$$

The bar over the electron-phonon matrix element denotes an angular average with respect to the direction of the parallel wave vector $\vec{q}_\parallel$; all other quantities in Eq. (9) are independent of the direction of $\vec{q}_\parallel$. Equation (9) is a particularly convenient form for numerical evaluation.

The temperature dependence of P arises from the Bose factors and through $\chi''(\vec{q},\omega)$. For a strongly degenerate Fermi system the latter is only weakly temperature dependent, in which case the energy-loss rate is well approximated by

$$P=F(T_e)-F(T_{\rm ph})\ , \tag{10}$$

where $F(T)$ exhibits a temperature dependence characteristic of the specific electron-phonon interaction being considered. The form of Eq. (10) reflects the fact that the net energy-transfer rate is the difference between phonon emission by the electrons at temperature T_e and phonon absorption from the lattice at temperature $T_{\rm ph}$. Since $F(T)$ is in general a rapidly increasing function of T, P will be dominated by $F(T_e)$ when T_e is appreciably larger than $T_{\rm ph}$.

The limiting low-temperature behavior of $F(T)$ can be extracted easily from Eq. (9) for each of the electron-phonon interactions (see the Appendix). For the deformation-potential interaction the electron-phonon matrix element is[19]

$$\overline{|M_{\vec{q}l}^{\rm DP}|^2}=\frac{\hbar Z^2}{2\rho s_l}q\ , \tag{11}$$

where ρ is the mass density of the solid, s_l is the longitudinal sound speed, and Z is the deformation-potential coupling constant. In the Debye model, only longitudinal modes contribute to the crystal dilation and hence to the coupling to electrons. The important point to note is the linear proportionality to q. Both longitudinal and transverse modes contribute in the piezoelectric interaction[20,21] and we have, for the respective cases, the averaged matrix elements[4]

$$\overline{|M_{\vec{q}l}^{\rm PZ}|^2}=\frac{\hbar(eh_{14})^2}{2\rho s_l}\frac{9q_\perp^2 q_\parallel^4}{2q^7} \tag{12}$$

and

$$\overline{|M_{\vec{q}t}^{\rm PZ}|^2}=\frac{\hbar(eh_{14})^2}{2\rho s_t}\frac{8q_\perp^4 q_\parallel^2+q_\parallel^6}{2q^7}\ , \tag{13}$$

where (eh_{14}) is the piezoelectric coupling constant. Both of these expressions behave as q^{-1} for small wave vectors. Thus, if the frequency wave-vector dependence of $\chi''(\vec{q},\omega)$ in Eq. (9) scales as $\omega^{n+m}q^{-m}$, we find the limiting low-temperature behaviors of $F^{\rm DP}(T)\propto T^{n+5}$ and $F^{\rm PZ}(T)\propto T^{n+3}$, i.e., T^7 and T^5, respectively, if $n=2$ as is found to be the case for screened electron-phonon interactions. This shows that the piezoelectric interaction dominates the energy-loss rate at low temperatures. However, the range of temperature over which these limiting forms are valid necessitates a more careful evaluation of Eq. (9). We note in passing that for optic modes, $F(T)\propto e^{-\hbar\omega_0/k_B T}$, which is small at temperatures well below the optic-mode frequency ω_0.

To this point we have not specified the electronic system and in fact Eq. (9) is perfectly general to within the approximate treatment of the phonons and their coupling to the electrons. The function $\chi''(\vec{q},\omega)$ is related to the density response function[22]

$$\chi(\vec{r},\vec{r}',t)=\frac{i}{\hbar}\Theta(t)\langle[\hat{n}(\vec{r},t),\hat{n}(\vec{r}',0)]\rangle\ , \tag{14}$$

which is defined in terms of the Heisenberg electron-density operators $\hat{n}(\vec{r},t)$. The quantity of interest is

$$\chi''(\vec{q},\omega)=\mathrm{Im}\int d^3r\int d^3r'\int dt\, e^{i\vec{q}\cdot(\vec{r}-\vec{r}')}e^{-i\omega t}\chi(\vec{r},\vec{r}',t)\ , \tag{15}$$

with $\vec{q}$ a three-dimensional wave vector. For a planar heterojunction, $\chi(\vec{r},\vec{r}',t)$ depends on the spatial variables z,z' and the difference $\vec{\rho}-\vec{\rho}'$. As a result, Eq. (15) reduces to

$$\chi''(\vec{q},\omega)=A\ \mathrm{Im}\int dz\int dz' e^{iq_\perp(z-z')}\chi(z,z',q_\parallel,\omega)\ , \tag{16}$$

where A is the area of the heterojunction interface.

To proceed, we make use of the random-phase approximation (RPA) in which the electrons are assumed to respond as independent particles to the total electrostatic potential.

A standard calculation then gives χ in the form

$$\chi(z,z',q_\parallel,\omega)=\sum_{\alpha,\beta}f_\alpha(z)f_\beta(z')\chi_\alpha^0(q_\parallel,\omega)\epsilon_{\alpha\beta}^{-1}(q_\parallel,\omega) \equiv\sum_{\alpha,\beta}f_\alpha(z)f_\beta(z')\chi_{\alpha\beta}(q_\parallel,\omega)\ , \tag{17}$$

where α denotes a pair of subband indices (n,n') and the summations run over all pairs of subband states of the heterojunction. These states appear in the form of the products

$$f_\alpha(z)=\varphi_n(z)\varphi_{n'}(z) . \tag{18}$$

The function $\chi^0_\alpha(q_\parallel,\omega)$ is a subband density polarization function defined by[23]

$$\chi^0_{nn'}(q_\parallel,\omega)=\frac{2}{A}\sum_{\vec{k}}\frac{f(\varepsilon_{n',\vec{k}+\vec{q}_\parallel})-f(\varepsilon_{n\vec{k}})}{\hbar\omega+i\delta+\varepsilon_{n\vec{k}}-\varepsilon_{n',\vec{k}+\vec{q}_\parallel}} , \tag{19}$$

where $\vec{k}$ is a two-dimensional wave vector and $\varepsilon_{n\vec{k}}=E_n+\hbar^2k^2/2m^*$ is the energy of the subband states. $f(\varepsilon)$ is the Fermi-Dirac distribution. The summation over $\vec{k}$ can be performed analytically at zero temperature while convenient integral expressions are available at finite temperature.[24] We shall not display these here as they are not needed in their full generality. Finally, the dielectric matrix is given by

$$\epsilon_{\alpha\beta}(q_\parallel,\omega)=\delta_{\alpha\beta}+V_{\alpha\beta}(q_\parallel)\chi^0_\beta(q_\parallel,\omega) , \tag{20}$$

where the Coulomb potential matrix element is defined by

$$V_{\alpha\beta}(q_\parallel)=\frac{2\pi e^2}{\kappa q_\parallel}\int dz\int dz' f_\alpha(z)f_\beta(z')e^{-q_\parallel|z-z'|} . \tag{21}$$

κ is the dielectric constant of GaAs.

Substituting these expressions into Eq. (16), we obtain

$$\chi''(\vec{q},\omega)=A\ \mathrm{Im}\sum_{\alpha,\beta}I^*_\alpha(q_\perp)I_\beta(q_\perp)\chi_{\alpha\beta}(q_\parallel,\omega) , \tag{22}$$

where we have defined the transition form factors

$$I_\alpha(q_\perp)=\int dz\, e^{-iq_\perp z}f_\alpha(z) . \tag{23}$$

In a matrix notation, χ is defined by the equation

$$\chi=\chi^0-\chi^0\mathbf{V}\chi . \tag{24}$$

Using this equation, we have

$$\chi\mathbf{I}=\chi^0\mathbf{J} , \tag{25}$$

where $\mathbf{I}$ is a column vector with components I_α and $\mathbf{J}$ is given by

$$\mathbf{J}=\epsilon^{-1}\mathbf{I} . \tag{26}$$

As a result, we find

$$\chi''(\vec{q},\omega)=A\ \mathrm{Im}[\mathbf{I}^*\chi\mathbf{I}]=A\ \mathrm{Im}[\mathbf{I}^*\chi^0\mathbf{J}]=A\ \mathrm{Im}\sum_\alpha I^*_\alpha\chi^0_\alpha J_\alpha , \tag{27}$$

since χ^0 is a diagonal matrix (with respect to the *pair* indices α). Equation (27) can finally be simplified as follows:

$$\begin{aligned}\chi''(\vec{q},\omega)&=\frac{A}{2i}\sum_\alpha(I^*_\alpha\chi^0_\alpha J_\alpha-I_\alpha\chi^{0*}_\alpha J^*_\alpha)\\&=\frac{A}{2i}\sum_\alpha[(\mathbf{J}+\mathbf{V}\chi^0\mathbf{J})^*_\alpha\chi^0_\alpha J_\alpha-(\mathbf{J}+\mathbf{V}\chi^0\mathbf{J})_\alpha\chi^0_\alpha J^*_\alpha]\\&=\frac{A}{2i}\sum_\alpha(J^*_\alpha\chi^0_\alpha J_\alpha-J_\alpha\chi^{0*}_\alpha J^*_\alpha)\\&=A\sum_\alpha|J_\alpha|^2\mathrm{Im}\chi^0_\alpha(q_\parallel,\omega) .\end{aligned} \tag{28}$$

There are two distinct contributions to Eq. (28). The first corresponds to single-particle excitations and occurs when $\mathrm{Im}\chi^0_\alpha$ is finite. This contribution is weighted by the screened transition form factors as can be seen from Eq. (26). There is also a second contribution which arises from the poles of $|J_\alpha|^2$ and corresponds to collective excitations, such as plasmons, of the electronic system. These, however, give a minor contribution to the energy-transfer rate at low temperatures and only the single-particle excitations need be considered.

Referring to Eq. (19), we have, for the imaginary part of χ^0_α, the expression

$$\begin{aligned}\mathrm{Im}\chi^0_{nn'}(q_\parallel,\omega)&=\frac{2\pi}{A}\sum_{\vec{k}}[f(\varepsilon_{n\vec{k}}-f(\varepsilon_{n',\vec{k}+\vec{q}_\parallel})]\\&\quad\times\delta(\hbar\omega+\varepsilon_{n\vec{k}}-\varepsilon_{n',\vec{k}+\vec{q}_\parallel})\\&=\frac{m^*}{2\pi\hbar^2}\frac{1}{\sqrt{\varepsilon_{q_\parallel}}}\int_{\varepsilon_{nn'}}^{\infty}d\varepsilon\frac{f(\varepsilon)-f(\varepsilon+\hbar\omega)}{\sqrt{\varepsilon-\varepsilon_{nn'}}} ,\end{aligned} \tag{29}$$

where

$$\varepsilon_{nn'}=E_n+\frac{(\hbar\omega+\Delta_{nn'}-\varepsilon_{q_\parallel})^2}{4\varepsilon_{q_\parallel}} , \tag{30}$$

with $\varepsilon_{q_\parallel}=\hbar^2q^2_\parallel/2m^*$ and $\Delta_{nn'}=E_n-E_{n'}$. At finite temperatures, Eq. (29) must be evaluated numerically but at zero temperature we have the analytic result

$$\begin{aligned}&\mathrm{Im}\chi^0_{nn'}(q_\parallel,\omega)|_{T=0}\\&=\frac{m^*}{\pi\hbar^2}\frac{1}{\sqrt{\varepsilon_{q_\parallel}}}[\Theta(E_F-\varepsilon_{nn'})\sqrt{E_F-\varepsilon_{nn'}}\\&\quad-\Theta(E_F-\hbar\omega-\varepsilon_{nn'})\sqrt{E_F-\hbar\omega-\varepsilon_{nn'}}].\end{aligned} \tag{31}$$

This expression reflects the nature of the electron-hole-pair excitations in the multisubband situation. The negative, second term accounts for the Pauli exclusion effect and corrects the spectral density for transitions to final states that are already occupied. From Eq. (29), these excitations occur at the energies

$$\begin{aligned}\hbar\omega&=\varepsilon_{n',\vec{k}+\vec{q}_\parallel}-\varepsilon_{n\vec{k}}\\&=\Delta_{n'n}+\frac{\hbar^2}{2m^*}(2\vec{k}\cdot\vec{q}_\parallel+q^2_\parallel) ,\end{aligned} \tag{32}$$

which defines a region in the ω-$q_\parallel$ plane corresponding to the occupied $\vec{k}$ states. Figure 2 shows the allowed excitations for a two-band model in which only the first subband is occupied ($E_1 < E_F$); intersubband excitations occur only above the minimum energy $\Delta_{10} - E_F$. As the occupancy of the first subband increases, the intersubband particle-hole spectrum slides down the ω axis, making intersubband excitations more accessible. From Eq. (9) we see that the region of the ω-$q_\parallel$ plane sampled in the energy-loss rate lies above the line $\omega = s_\lambda q_\parallel$ and is cut off above some frequency ω of the order $k_B T/\hbar$ because of the Bose factors. Thus intersubband excitations first begin to contribute when $\Delta_{10} - E_F \sim k_B T$. Once the second subband is occupied, excitations from the second subband also occur and are represented by the $\mathrm{Im}\chi^0_{10}$ and $\mathrm{Im}\chi^0_{11}$ terms in Eq. (31). The particle-hole excitation spectrum is illustrated in Figs. 3(a) and 3(b) for transitions from the first and second subbands, respectively.

With the result given in Eq. (28), our final expression for the energy-loss rate is

$$P = \frac{1}{n_T} \int_0^\infty d\omega\, \omega^2 [N_e(\omega) - N_{\mathrm{ph}}(\omega)] \times \sum_\lambda \frac{1}{s_\lambda \pi^2} \int_0^{\omega/s_\lambda} dq_\parallel \frac{q_\parallel}{(\omega^2 - s_\lambda^2 q_\parallel^2)^{1/2}} \times \overline{|M_{\vec{q}\lambda}|^2} \sum_\alpha |J_\alpha(q_\parallel, q_\perp, \omega)|^2 \times \mathrm{Im}\chi^0_\alpha(q_\parallel, \omega) , \tag{33}$$

where n_T is the *total* electron areal density. $\mathrm{Im}\chi^0_\alpha$ was evaluated using Eq. (29), and all integrals were performed numerically for each of the electron-phonon matrix elements in Eqs. (11)–(13). At the low temperatures of interest, the integrals are restricted to low frequencies. A typical parallel wave vector is such that $v_F q_\parallel \sim (v_F/s_\lambda)\omega \gg \omega$, where v_F is the electronic Fermi velocity. As a result, electronic screening is essentially static and the $\omega = 0$ limit of the dielectric matrix provides a good approximation in the screened form factors, Eq. (26). Finally, we have retained only the lowest two subbands in the calculation of the screened form factors. The effect of the second subband is included in the first-subband polarization, even when just the first subband is occupied.

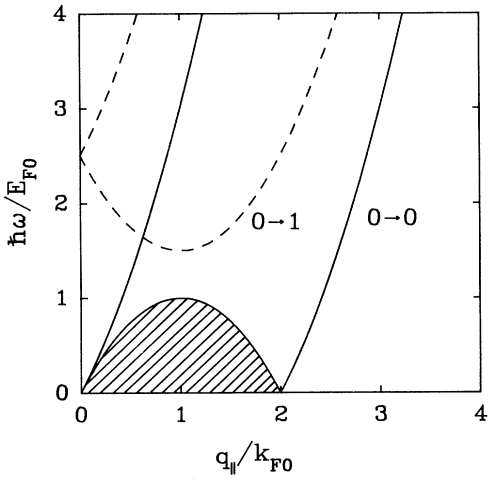

FIG. 2. Domain of the particle-hole excitation spectrum for a subband occupancy corresponding to $\Delta_{10}/E_{F0} = 2.5$. The notation $n \to n'$ indicates transitions from the nth to n'th subband. The region bounded by the solid (dashed) lines is that for which the transition $0 \to 0$ ($0 \to 1$) is allowed. The shaded region indicates the range of variables in which the Pauli exclusion effect is operative for the $0 \to 0$ transition.

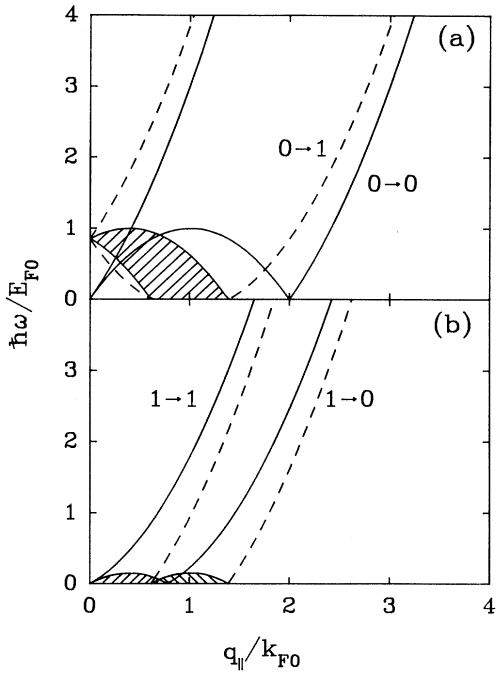

FIG. 3. As for Fig. 2, but with $\Delta_{10}/E_{F0} = 0.85$ corresponding to two-subband occupancy. Panel (a) is for excitations from the lower subband. For clarity we have shaded only the region for the $0 \to 1$ transition in which the Pauli principle has an effect; the situation for the $0 \to 0$ transition is the same as Fig. 2. Panel (b) corresponds to excitations starting from the upper subband. Again, the shaded regions indicate where the Pauli principle has an effect.

The only place in which the subband wave functions appear explicitly is in the transition form factors, Eq. (23). The wave functions were obtained from a self-consistent calculation of the heterojunction electronic structure as described in a previous paper.[11] The calculations were performed for each 2D EG density in accord with the experimental conditions of persistent photoconductivity, i.e., those pertaining to infrared irradiation. From our earlier work it is known that the electronic structure is well described theoretically for the full range of areal densities and we therefore expect our transition form factors to represent faithfully the actual situation.

The results of our calculations of the temperature dependence are displayed in Figs. 4 and 5 for a fixed den-

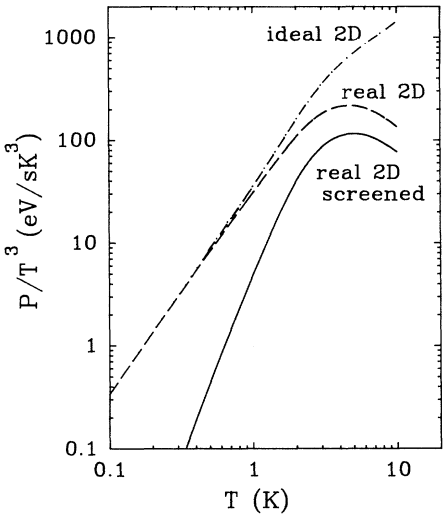

FIG. 4. The calculated deformation-potential contribution to the energy-loss rate $P=F(T)$ as a function of T in the present sample (i.e., with $T_{\rm ph}=0$ K so $T\equiv T_e$) and $n_T=5.5\times10^{15}$ m^{-2}. The dashed-dotted and dashed lines do not include electronic screening; the dashed-dotted line is for an ideal 2D gas of arbitrarily small thickness while the dashed line is calculated with the actual wave function of the 2D gas. The solid line gives the final result which includes both screening and form-factor effects.

sity of $n_T=5.5\times10^{15}$ m^{-2} corresponding to a single occupied subband. In these calculations we have used the following material parameters: $m^*=0.067m_e$, $\kappa=13.2$, $s_l=5.12\times10^3$ m s^{-1}, $s_t=3.01\times10^3$ m s^{-1}, $\rho=5.36$ g cm^{-3}, $Z=10$ eV, and $eh_{14}=0.12$ eV Å^{-1}. In Fig. 4 we show the effect of making various approximations in the calculation of $F(T)$ for the deformation-potential coupling. First, we have neglected the screened form factor in Eq. (33) which corresponds to assuming an ideal 2D EG with no electronic interactions; next, we include the actual form factors, calculated with the self-consistent wave functions, but still assuming no interactions; and, finally, we include both screening and form-factor effects. The argument of the form factor $I_{00}(q_\perp)$ is

$$q_\perp=[(\omega/s_\lambda)^2-q_\parallel^2]^{1/2}\ ,$$

which is small for small frequencies. Thus at low temperatures, $I_{00}(q_\perp)$ approaches unity, which explains why the "ideal 2D" and "real 2D" curves merge in this limit. The characteristic power law for the unscreened-deformation-potential coupling is T^5 (see the Appendix). At higher temperatures, the parameter $aq_\perp$ (where a is the typical extent of the subband wave function) becomes appreciable over the range of integration and $|I_{00}(q_\perp)|^2$ falls below unity, leading to a reduction in the energy-loss rate. When screening is included, $|I_{00}|^2$ is reduced by an additional factor of $[\epsilon_{00}(q_\parallel,0)]^{-2}$. It should be emphasized in this regard that physically there is no choice in the matter; screening of the interactions *must* be included. Since the static dielectric function is given by

$$[\epsilon_{00}(q_\parallel,0)]^{-1}=q_\parallel/(q_\parallel+q_s)\ ,$$

where q_s is the screening wave vector, the integrand in Eq. (33) acquires an additional factor of $q_\parallel^2$ which changes the low-temperature power law to T^7; this is seen to become effective below about 1 K. In the range of temperatures between 2 and 10 K, $F(T)/T^3$ is relatively constant so that an apparent T^3 law is observed. However, this is just the transition region from the low- (Bloch) to high-temperature behaviors and is not a characteristic limiting form.

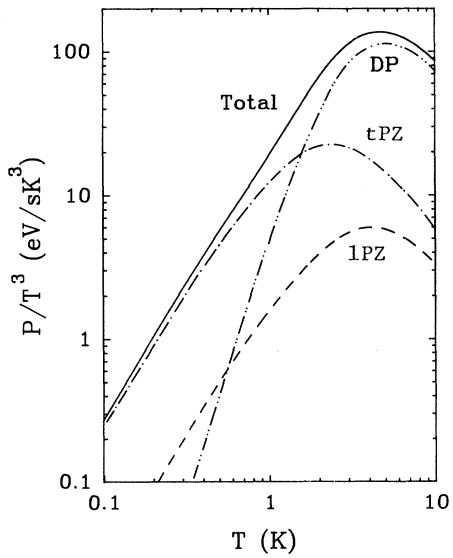

FIG. 5. The calculated energy-loss rate $P=F(T)$ as a function of T for the present sample with $n_T=5.5\times10^{15}$ m^{-2} (i.e., with $T_{\rm ph}=0$ K so $T\equiv T_e$). The various dashed lines show the contributions from deformation potential (DP), transverse piezoelectric (tPZ), and longitudinal piezoelectric (lPZ) scattering to the total (solid line).

In Fig. 5 we compare the relative contributions to the energy-loss rate of the deformation-potential and piezoelectric interactions. The transverse component, Eq. (13), exceeds the longitudinal component throughout the temperature range shown, mainly because of its lower sound speed. Since the screened piezoelectric interaction leads to a limiting T^5 low-temperature behavior, it dominates the deformation-potential coupling below about 2 K. At higher temperatures, the piezoelectric contribution is typically a 10% correction. Interestingly, because of the relative magnitudes of the deformation-potential and piezoelectric contributions, the low-temperature T^5 law extends to somewhat higher temperatures than for the piezoelectric contribution alone. We shall return to a more detailed comparison with experiment in Sec. IV.

IV. RESULTS AND DISCUSSION

It is convenient to present the data in the form of the power P required to produce a fixed temperature T_e at a constant lattice temperature $T_{\rm ph}$. In order to do this, we have interpolated the original experimental data sets (containing about 17 different T_e at each n_T) to produce data at a few selected T_e as shown in Fig. 6. The results

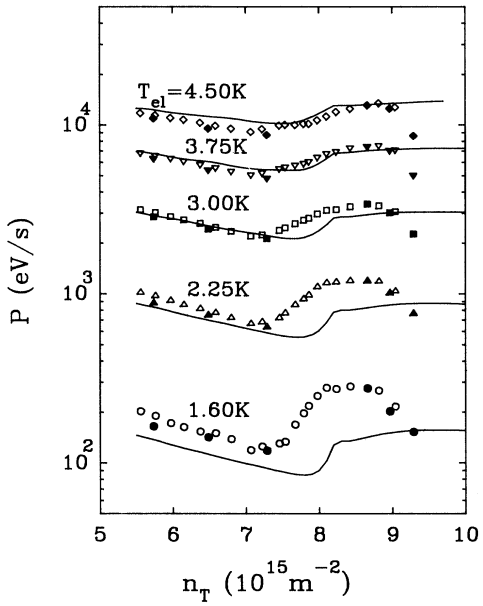

FIG. 6. The measured (symbols) and calculated (solid lines) energy-loss rates $P=F(T_e)-F(T_{ph})$ as a function of total electron density n_T. The measured data have been interpolated from much larger data sets to give P at various fixed T_e. All the data are appropriate to $T_{ph}=1.17$ K. The solid and open symbols on each data set correspond to different experimental runs.

of the calculations are also displayed for comparison; the only adjustable parameters in the calculations are the deformation-potential coupling constant Z and the piezoelectric coupling eh_{14}. Over most of the temperature range Z is mainly responsible for the observed magnitudes and it is clear that we could not significantly change our value of $Z=10$ eV without seriously affecting the quality of the experimental and theoretical agreement. Recalling that the energy-loss rate for deformation-potential scattering varies as Z^2, we see that the value of Z at 10 eV is probably accurate to $\pm 10\%$. This value is in good agreement with 11 ± 1 eV deduced by Hirakawa and Sakaki[3] for MBE samples with energy-loss rates measured over the range 4–20 K and is in agreement with a recent estimate of $Z=9.3$ eV for bulk GaAs.[25] This suggests that the model of the bulk acoustic waves interacting with the 2D EG is adequate to completely explain the energy-loss rates and no further mechanisms need be invoked. The higher value of 16 eV obtained by Manion *et al.*[4] over the range 3–7 K was obtained with a metal-organic chemical-vapor deposition (MOCVD) sample, which may be a relevant factor.

The qualitative density dependence of the observed energy-loss rate is well reproduced by the theory and the agreement is particularly good at the higher electron temperatures. For single subband occupancy, the low-temperature density dependence is $n_T^{-3/2}$ (from the factor k_F^{-3}; see the Appendix) which accounts quite well for the decreasing trend in the range of densities from 5.5×10^{15} to $(7.5\times 10^{15}$ m^{-2}. Beyond about 7.5×10^{15} m^{-2}, there is a sudden increase in the dissipation rate due to the onset of inelastic intersubband scattering. The differences between theory and experiment in the range $(7.5-8.5)\times 10^{15}$ m^{-2} have two sources. First, the second subband becomes occupied theoretically at a density of 8.3×10^{15} m^{-2} whereas experimentally it is closer to 8.0×10^{15} m^{-2}. Thus the onset of intersubband scattering should occur somewhat later in the theory. This difference can be eliminated by a slight adjustment of the acceptor areal density from 0.73×10^{15} to 0.70×10^{15} m^{-2} but we have chosen, for purposes of comparison, to retain the value of 0.73×10^{15} m^{-2}, which is obtained directly from experiment.[11]

The second source of difference between theory and experiment is due to the different threshold behaviors of the second-subband density of states. In our calculations we have assumed an ideal 2D density of states while the actual subband edge is impurity broadened. The latter effect is clearly evident in this sample in measurements of the mobility[11] and in (unpublished) measurements using magnetic depopulation. Referring to Fig. 3, there is not in reality a sharp boundary defining the single-particle excitation spectrum for the intersubband excitations. As a result, excitations into the second subband can occur at a lower density as the Fermi level begins to enter the tail of the second-subband density of states. There is an additional thermal smearing effect which is clearly seen in the calculations and which increases the experimental width of the transition region at elevated temperatures.

There are in addition two discrepancies for which we have no explanation. The increase of the intersubband scattering contribution to the energy-loss rate is more pronounced in the experimental results than in the theory at the lowest electron temperatures. Secondly, the experimental energy-loss rates begin to decrease as the density approaches the saturation density of the heterojunction while theory indicates that a plateau is maintained up to a value of $n_T=10\times 10^{15}$ m^{-2}. However, there is a greater uncertainty in the experimental values at the highest densities and the observed falloff is not well established experimentally. In spite of these differences, the agreement between theory and experiment is gratifying and supports the soundness of the theoretical formulation.

We also compare calculations and experiment at a fixed n_T as a function of T_e. This is most useful if we correct the experimental data to $T_{ph}=0$, i.e., by producing $F(T_e)=P+F(T_{ph})$. In this case we can compare directly with the calculated characteristic function $F(T)$ as discussed in Sec. II. We do this by assuming $F(T)=\alpha T^{\gamma}$ with $\gamma\approx 5$ for $T<2$ K (cf. Fig. 5). We then use

$$F(T_{ph})=P/[(T_e/T_{ph})^{\gamma}-1]\ ,$$

where P is the measured energy-loss rate measured at T_e and T_{ph}. We typically have three data points below 2 K which enables three independent values of $F(T_{ph})$ to be estimated. We find $F(T_{ph})$ to be in the range 30–50 eV s^{-1} with a maximum uncertainty of 20% for any particular value. After correcting for $F(T_{ph})$, we produce data sets for $F(T_e)\equiv F(T)$ of which three examples are

shown in Fig. 7. We avoided the region where the second subband is just appearing because, as we have already mentioned, the observed width of this region is clearly dominated by disorder broadening but the calculations do not attempt to take this into account. Again, the overall agreement is good in both the trend of the results and the absolute magnitudes. Notice that in this figure most of the temperature variation is removed by plotting $F(T)/T^3$ and so we are looking at deviations from $F(T)\sim T^3$. In particular, we see that the cubic power law is approximately valid at higher temperatures and explains why the bulk of the published experimental data in the liquid-^{4}He temperature range appears to follow this law. To emphasize this, Fig. 8 shows data plotted in the style that has become common in the literature,[8] i.e., $\ln P$ as a function of $\ln(T_e^3-T_{\rm ph}^3)$. This plot indicates that the cubic power law is not unreasonable though there are systematic deviations from the line that has a slope of unity. The tendency for $F(T)/T^3$ to tend to the origin in Fig. 7 seems to be the first demonstration of the smooth transition from medium- to low-temperature behavior, and indicates the onset of $F(T)\sim T^5$ at the lowest temperatures. In connection with this, Wennberg *et al.*[10] have obtained the expected $F(T)=\alpha T^5$ behavior on a superlattice at $T\leq 0.1$ K and have evaluated α. If we use their results to calculate $F(T)/T^3$ at 0.1 K, we obtain 0.020 eV/s K^3 at an electron density of 1.7×10^{15} m^{-2}. The calculated value for our sample at the lowest density of 5.5×10^{15} m^{-2} (see Fig. 5) is about 0.3 eV/s K^3, and this will increase somewhat at lower n_T according to the trends shown in Fig. 6 and discussed in Sec. IV and the Appendix, i.e., $F(T)\sim n_T^{-3/2}$. In other words the energy-loss rates reported by Wennberg *et al.* seem to be at least an order of magnitude lower than we would expect, a conclusion which echoes their own statements on the matter.

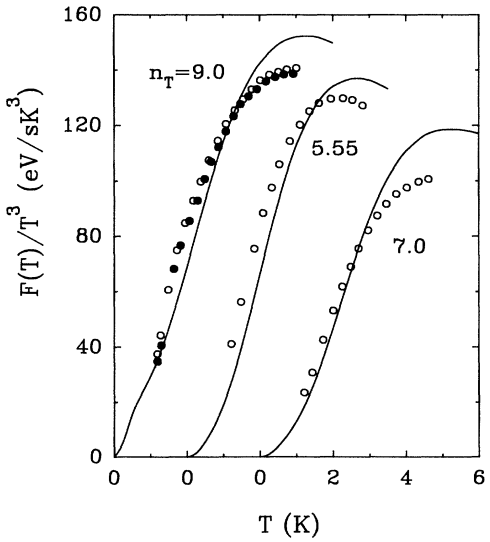

FIG. 7. The energy-loss rates as a function of electron temperature T_e for the three fixed electron densities n_T (in units of 10^{15} m^{-2}). Both the experimental and theoretical curves are for $T_{\rm ph}=0$ K and so $P=F(T_e)\equiv F(T)$. The experimental data have been corrected for $F(T_{\rm ph})$ as outlined in the text. In the case of $n_T=9.0\times10^{15}$ m^{-2}, there are two independent sets of experimental data at $n_T=9.04\times10^{15}$ m^{-2} (open circles) and $n_T=8.97\times10^{15}$ m^{-2} (solid circles).

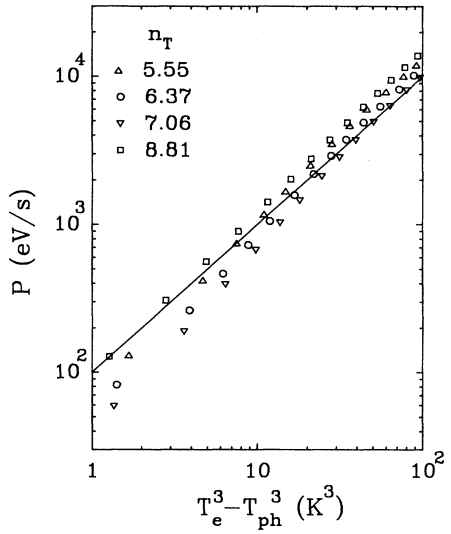

FIG. 8. Typical data on energy-loss rate P as a function of $T_e^3-T_{\rm ph}^3$ for particular values of n_T (in units 10^{15} m^{-2}). In all cases $T_{\rm ph}=1.17$ K. The solid line has a slope of unity.

With reference to Fig. 5, we see that, at the lowest electron temperature achieved in our experiments ($T_e=1.6$ K), the deformation-potential and piezoelectric coupling contributions are comparable. It would be of considerable interest to extend these measurements to lower temperatures where the piezoelectric interaction is dominant. It would then be possible to check the magnitude of the piezoelectric coupling constant.

V. CONCLUSIONS

Using deformation-potential and piezoelectric coupling parameters consistent with bulk GaAs values, we have been able to give a good account of both the temperature dependence and the electron-density dependence of the electronic energy-loss rate for a well-characterized sample in the liquid-^{4}He temperature range. This, together with the similar results of Hirakawa and Sakaki[3] in the 4–20-K range, suggests that the interaction of bulk lattice waves with the 2D EG provides an adequate description of the experiments and no other scattering mechanisms need be invoked at the present time. We can roughly represent our data using a T^3 dependence for the energy-loss rate, as has been observed by many others. However, below about 3 K we see a transition to a higher power law, in accord with the theoretical calculations. Although the limiting low-temperature behavior of T^5 appropriate to piezoelectric electron-phonon scattering becomes valid only below about 1 K, theory shows that the combination of deformation-potential and piezoelectric scattering behaves approximately as T^5 to about 2 K and this is presumably what we are observing. At about 1.5 K, both types of scattering have roughly equal magnitude and so one needs temperatures of ≤ 1 K to investigate the piezoelectric part in isolation. The apparent T^3 dependence of the energy-loss rate over most of the

liquid-^{4}He temperature range is seen to be of no fundamental significance and represents a transition region between the T^5 low-temperature limit and a variation of roughly T^2 by 10 K.

The occupation of the second subband is readily visible in both the experimental and theoretical results. Roughly speaking, the strong rise in the energy-loss rate at this point is due to the enhancement of the electron-phonon scattering rate by the increased density of states. Kreschuk *et al.*[7] reported a change in the power law from T^3 to T^2 as the second subband becomes occupied but we do not see any comparable effect in either the theory or the experiments.

ACKNOWLEDGMENTS

This work was partially supported by grants from the Natural Sciences and Engineering Research Council of Canada.

APPENDIX

In this appendix we consider the single-subband model and obtain the limiting low-temperature behavior of the electron-energy-loss rates for the various kinds of electron-phonon interactions. For this purpose it is sufficient to use the $T=0$ K form of $\mathrm{Im}\chi^0_{nn'}$ in Eq. (31), expanded to leading order in ω,

$$\mathrm{Im}\chi^0_{00}(q_\parallel,\omega)=\frac{m^*}{\pi\hbar^2}\frac{\omega}{v_F q_\parallel}\frac{\Theta(E_F-\varepsilon_{00})}{\left[1-\dfrac{\varepsilon_{00}}{E_F}\right]^{1/2}}, \tag{A1}$$

where ε_{00} is given in Eq. (30). Substituting this expression in Eq. (33), we have

$$F(T)=\frac{2m^{*2}}{\pi^2\hbar^3 k_F^3}\int_0^\infty d\omega\,\omega^3 N(\omega)\sum_\lambda\frac{1}{s_\lambda}\int_0^{\omega/s_\lambda}dq_\parallel\frac{\overline{|M_{\vec{q}\lambda}|}^2}{(\omega^2-s_\lambda^2 q_\parallel^2)^{1/2}}\frac{|I_{00}(q_\perp)|^2}{[\epsilon(q_\parallel)]^2}\frac{\Theta(E_F-\varepsilon_{00})}{\left[1-\dfrac{\varepsilon_{00}}{E_F}\right]^{1/2}}. \tag{A2}$$

In the limit of low temperatures $|I_{00}(q_\perp)|^2$ can be set equal to unity and the static dielectric function is given (for $q_\parallel<2k_F$) by

$$\epsilon(q_\parallel)=1+\frac{q_s}{q_\parallel}, \tag{A3}$$

where $q_s=2m^*e^2/\kappa\hbar^2$ is the screening wave vector, in cgs units.

We consider first the deformation-potential interaction for which $|M_{\vec{q}l}^{\mathrm{DP}}|^2=\hbar Z^2\omega/2\rho s_l^2$ is independent of $q_\parallel$. The basic $q_\parallel$ integral to be considered is therefore

$$I\equiv\int_0^{\omega/s}dq_\parallel\frac{\epsilon^{-2}(q_\parallel)}{(\omega^2-s^2q_\parallel^2)^{1/2}}\frac{\Theta(E_F-\varepsilon_{00})}{\left[1-\dfrac{\varepsilon_{00}}{E_F}\right]^{1/2}}, \tag{A4}$$

where s is a phonon sound speed. The result for $\epsilon(q_\parallel)=1$ will be denoted I_{unscr} while the result obtained using (A3) will be denoted I_{scr}. With the substitution $q_\parallel=(\omega/s)u$, we have

$$I_{\mathrm{unscr}}=\frac{1}{s}\int_0^1 du\frac{1}{(1-u^2)^{1/2}}\frac{\Theta(E_F-\epsilon_{00})}{\left[1-\dfrac{\epsilon_{00}}{E_F}\right]^{1/2}}. \tag{A5}$$

The domain of integration is restricted by the Θ function: setting ε_{00} equal to E_F, we obtain the equation

$$u^2=\frac{m^*s^2}{2E_F}\left[1-\frac{\hbar\omega}{2m^*s^2}u^2\right]^2. \tag{A6}$$

Defining

$$t^2=\frac{\hbar\omega}{2m^*s^2}u^2 \tag{A7}$$

and

$$\gamma^2=\frac{\hbar\omega}{4E_F}, \tag{A8}$$

Eq. (A6) can be written as

$$t^2=\gamma^2(1-t^2)^2, \tag{A9}$$

which has the positive roots

$$t_1=\frac{\sqrt{1+4\gamma^2}-1}{2\gamma},\quad t_2=\frac{\sqrt{1+4\gamma^2}+1}{2\gamma}. \tag{A10}$$

Since γ is a small parameter at low temperatures, we have

$$t_1\simeq\gamma\quad\text{and}\quad t_2\simeq 1/\gamma, \tag{A11}$$

so that the integration range in (A5) is bounded by

$$u_1=\left[\frac{2m^*s^2}{\hbar\omega}\right]^{1/2}t_1=\left[\frac{m^*s^2}{2E_F}\right]^{1/2}=\frac{s}{v_F} \tag{A12}$$

and

$$u_2=\left[\frac{2m^*s^2}{\hbar\omega}\right]^{1/2}t_2=\frac{(8m^*s^2E_F)^{1/2}}{\hbar\omega}=\frac{2k_F}{q}. \tag{A13}$$

If $q<2k_F$, u_2 is larger than 1 and the upper limit of integration in (A5) remains unaffected. Thus in this limit we have

$$I_{\rm unscr}=\frac{u_2}{s}\int_{u_1}^{1}du\frac{u}{[(1-u^2)(u_2^2-u^2)(u^2-u_1^2)]^{1/2}}$$
$$\underset{u_2\to\infty}{\simeq}\frac{1}{s}\int_{u_1}^{1}du\frac{u}{[(1-u^2)(u^2-u_1^2)]^{1/2}}$$
$$=\frac{\pi}{2s}\ . \tag{A14}$$

We therefore find

$$F_{\rm unscr}^{\rm DP}(T)=\frac{2m^{*2}}{\pi^2\hbar^3k_F^3}\frac{\hbar Z^2}{2\rho s_l^3}\frac{\pi}{2s_l}\int_0^\infty d\omega\,\omega^4N(\omega)$$
$$=\frac{12\zeta(5)}{\pi}\frac{m^{*2}Z^2}{k_F^3\hbar^7\rho s_l^4}(k_BT)^5\ , \tag{A15}$$

where $\zeta(5)$ is the Riemann ζ function. Equation (A15) is identical to the result found by Karpus.[16] According to Eq. (A13), the low-temperature result is valid for

$$k_BT\ll(8m^*s_l^2E_F)^{1/2}\equiv k_BT_0\ .$$

For $n_T=5.5\times10^{15}\ {\rm m}^{-2}$, the characteristic temperature is $T_0=15$ K. As can be seen from Fig. 4, the low-temperature form is only valid when $T/T_0\le0.1$

When screening is included, the integrand in Eq. (A4) contains the additional factor $(q_\parallel/q_s)^2$ and, following a similar analysis,

$$I_{\rm scr}=\frac{\omega^2}{s^3q_s^2}\int_0^1du\frac{u^2}{(1-u^2)^{1/2}}\frac{\Theta(E_F-\varepsilon_{00})}{\left[1-\frac{\varepsilon_{00}}{E_F}\right]^{1/2}}$$
$$\simeq\frac{\pi}{4}\frac{\omega^2}{s^3q_s^2}\ . \tag{A16}$$

Thus we find

$$F_{\rm scr}^{\rm DP}(T)=\frac{180\zeta(7)}{\pi}\frac{m^{*2}Z^2}{k_F^3\hbar^9\rho s_l^6q_s^2}(k_BT)^7\ . \tag{A17}$$

For completeness, we list the screened and unscreened results for the longitudinal and transverse piezoelectric couplings,

$$F_{\rm unscr}^{\rm lPZ}(T)=\frac{9\zeta(3)}{32\pi}\frac{m^{*2}(eh_{14})^2}{k_F^3\hbar^5\rho s_t^2}(k_BT)^3\ , \tag{A18}$$

$$F_{\rm unscr}^{\rm tPZ}(T)=\frac{13\zeta(3)}{32\pi}\frac{m^{*2}(eh_{14})^2}{k_F^3\hbar^5\rho s_t^2}(k_BT)^3\ , \tag{A19}$$

$$F_{\rm scr}^{\rm lPZ}(T)=\frac{135\zeta(5)}{64\pi}\frac{m^{*2}(eh_{14})^2}{k_F^3\hbar^7\rho s_l^4q_s^2}(k_BT)^5\ , \tag{A20}$$

$$F_{\rm scr}^{\rm tPZ}(T)=\frac{177\zeta(5)}{64\pi}\frac{m^{*2}(eh_{14})^2}{k_F^3\hbar^7\rho s_t^4q_s^2}(k_BT)^5\ . \tag{A21}$$

[1] A. B. Fowler, F. F. Fang, W. E. Howard, and P. J. Stiles, Phys. Rev. Lett. **16**, 901 (1966).

[2] See, for example, W. Honlein and G. Landwehr, Solid State Commun. **51**, 679 (1984); Y. Kawaguchi and S. Kawaji, Jpn. J. Appl. Phys. **21**, L709 (1982); V. T. Dolgopolov, A. A. Shashkin, S. I. Dorozhkin, and E. A. Vyrodov, Zh. Eksp. Teor. Fiz. **89**, 2113 (1985) [Sov. Phys.—JETP **62**, 1219 (1985)].

[3] K. Hirakawa and H. Sakaki, Appl. Phys. Lett. **49**, 889 (1986).

[4] S. J. Manion, M. Artaki, M. A. Emanuel, J. J. Coleman, and K. Hess, Phys. Rev. B **35**, 9203 (1987).

[5] Y. Okuyama and N. Tokuda, Phys. Rev. B **40**, 9744 (1989).

[6] M. G. Blyumina, A. G. Denisov, T. A. Polyanskaya, I. G. Savel'ev, A. P. Senichkin, and Yu. V. Shmartsev, Pis'ma Zh. Eksp. Teor. Fiz. **44**, 257 (1986) [JETP Lett. **44**, 331 (1986)].

[7] A. M. Kreschuk, M. Yu. Martisov, T. A. Polyanskaya, I. G. Savel'ev, I. I. Saidashev, A. Ya. Shik, and Yu. V. Shmartsev, Solid State Commun. **65**, 1189 (1988).

[8] D. R. Leadley, R. J. Nicholas, J. J. Harris, and C. T. Foxon, Semicond. Sci. Technol. **4**, 879 (1989).

[9] M. J. Barlow, B. K. Ridley, M. J. Kane, and S. J. Bass, Solid-State Electron. **31**, 501 (1988).

[10] A. K. M. Wennberg, S. N. Ytterboe, C. M. Gould, H. M. Bozler, J. Klem, and H. Morkoç, Phys. Rev. B **34**, 4409 (1986).

[11] R. Fletcher, E. Zaremba, M. D'Iorio, C. T. Foxon, and J. J. Harris, Phys. Rev. B **41**, 10 649 (1990).

[12] Y. Ma, R. Fletcher, E. Zaremba, M. D'Iorio, C. T. Foxon, and J. J. Harris, Surf. Sci. **229**, 80 (1990).

[13] Sh. M. Kogan, Fiz. Tverd. Tela (Leningrad) **4**, 2474 (1962) [Sov. Phys.—Solid State **4**, 1813 (1963)].

[14] A. J. Leggett and M. Vuorio, J. Low Temp. Phys. **3**, 359 (1970).

[15] P. J. Price, J. Appl. Phys. **53**, 6863 (1982).

[16] V. Karpus, Fiz. Tekh. Poluprovodn. **20**, 12 (1986) [Sov. Phys.—Semicond. **20**, 6 (1986)].

[17] S. Adachi, J. Appl. Phys. **58**, R1 (1985).

[18] H. Ezawa, S. Kawaji, and K. Nakamura, Jpn. J. Appl. Phys. **13**, 126 (1974).

[19] C. Kittel, *Quantum Theory of Solids* (Wiley, New York, 1963).

[20] J. D. Zook, Phys. Rev. **136**, A869 (1964).

[21] G. Mahan, in *Polarons in Ionic Crystals and Polar Semiconductors,* edited by J. T. Devreese (North-Holland, Amsterdam, 1972), p. 553.

[22] P. C. Martin, in *Many-Body Physics,* edited by C. de Witt and R. Balian (Gordon and Breach, New York, 1968).

[23] See, for example, T. Ando, A. B. Fowler, and F. Stern, Rev. Mod. Phys. **54**, 437 (1984).

[24] P. F. Maldague, Surf. Sci. **73**, 296 (1978).

[25] D. D. Nolte, W. Walukiewicz, and E. E. Haller, Phys. Rev. Lett. **59**, 501 (1987).